Journal of Structural Biology 192 (2015) 461–469

Contents lists available at ScienceDirect

Journal of Structural Biology

journal homepage: www.elsevier.com/locate/yjsbi

Three-dimensional mass density mapping of cellular ultrastructure by ptychographic X-ray nanotomography

Ana Diaz [a,*], Barbora Malkova [a], Mirko Holler [a], Manuel Guizar-Sicairos [a], Enju Lima [b], Valerie Panneels [a], Gaia Pigino [c], Anne Greet Bittermann [d], Larissa Wettstein [a], Takashi Tomizaki [a], Oliver Bunk [a], Gebhard Schertler [a], Takashi Ishikawa [a], Roger Wepf [d], Andreas Menzel [a]

[a] Paul Scherrer Institut, 5232 Villigen PSI, Switzerland
[b] Brookhaven National Laboratory, 11973 Upton, NY, USA
[c] Max Planck Institute of Molecular Cell Biology and Genetics, 01307 Dresden, Germany
[d] Scientific Center for Optical and Electron Microscopy, ETH Zürich, 8093 Zurich, Switzerland

ARTICLE INFO

Article history:
Received 4 July 2015
Received in revised form 6 October 2015
Accepted 10 October 2015
Available online 22 October 2015

Keywords:
Ptychography
X-ray microscopy
Chlamydomonas

ABSTRACT

We demonstrate absolute quantitative mass density mapping in three dimensions of frozen-hydrated biological matter with an isotropic resolution of 180 nm. As model for a biological system we use *Chlamydomonas* cells in buffer solution confined in a microcapillary. We use ptychographic X-ray computed tomography to image the entire specimen, including the 18 μm-diameter capillary, thereby providing directly an absolute mass density measurement of biological matter with an uncertainty of about 6%. The resulting maps have sufficient contrast to distinguish cells from the surrounding ice and several organelles of different densities inside the cells. Organelles are identified by comparison with a stained, resin-embedded specimen, which can be compared with established transmission electron microscopy results. For some identified organelles, the knowledge of their elemental composition reduces the uncertainty of their mass density measurement down to 1% with values consistent with previous measurements of dry weight concentrations in thin cellular sections by scanning transmission electron microscopy. With prospects of improving the spatial resolution in the near future, we expect that the capability of non-destructive three-dimensional mapping of mass density in biological samples close to their native state becomes a valuable method for measuring the packing of organic matter on the nanoscale.

1. Introduction

The capability of visualizing with high resolution the three-dimensional (3D) structure of biological tissue has provided valuable insights into the cellular ultrastructure (Leis et al., 2009) and extracellular organization, e.g., of neural networks (Helmstaedter et al., 2008). With sufficient resolution to visualize cell membranes, electron microscopy (EM) is frequently used for imaging cellular ultrastructure. Cryo-fixation avoids radiation damage and sample movements during acquisition while keeping the specimen close to its native state (Adrian et al., 1984). Vitrification processes are used in such cases to prevent the creation of ice crystals which destroy the delicate cellular structure. However, the short penetration depth of electrons requires slicing, which can produce artifacts (Al-Amoudi et al., 2005).

Apart from the cellular structure information provided by images, physical quantities such as the mass density allow insight into the organization of molecules in the cellular matrix. This information is typically gained by density gradient centrifugation techniques, which usually require measurements of purified substances in vitro (Yoon and Lim, 2003). Some imaging techniques yield simultaneously spatially resolved structural information with quantitative mass density information. For example, the darkfield contrast in scanning transmission electron microscopy (STEM) of thin slices scales with the mass. This technique is used in combination with X-ray microanalysis to estimate weight concentrations of different substances in cellular compartments while they remain

* Corresponding author.
E-mail address: ana.diaz@psi.ch (A. Diaz).

http://dx.doi.org/10.1016/j.jsb.2015.10.008
1047-8477/

in their natural environment (von Zglinicki and Bimmler, 1987). Together with further biochemical and biophysical analysis, resolving in 3D the nanoscale density distribution could provide new valuable insight into molecular packing in cellular and extracellular compartments in context with the cell or tissue in which they are embedded.

Complementary to cryo-EM, cryo X-ray microscopy is capable of resolving cellular ultrastructure down to about 30 nm resolution (Parkinson et al., 2008; Schneider et al., 2010; Chichón et al., 2012; Hanssen et al., 2012). Typically used in absorption contrast at energies within the so-called water window, i.e., the energy range between absorption edges of carbon and oxygen, it provides high contrast between biological matter and water, facilitating 3D visualization of entire cells with thicknesses up to about 10 μm without sectioning. For samples thicker than 10 μm, the X-ray energy must be increased, and phase-sensitive X-ray microscopy concepts such as holo-tomography (Cloetens et al., 1999), Zernike phase contrast (Stampanoni et al., 2010), or coherent diffraction imaging (CDI) (Jiang et al., 2010) need to be used because of the reduced absorption contrast of biological tissues at such energies. Here one measures the phase shift of the X-ray wave field as it propagates through the sample as contrast mechanism instead of the attenuation of the wave field. Phase contrast is mostly related to the mass density variations within the specimen. Therefore, phase tomography offers the possibility to map the specimen's 3D mass density distribution on the nanoscale.

The technique of ptychographic X-ray computed tomography (PXCT) enables 3D density mapping of samples tens of micrometers in size with resolutions down to tens of nanometers (Dierolf et al., 2010). Ptychography is a CDI modality which consists of scanning a specimen across a confined coherent illumination in such a way that illuminated areas partially overlap at various scan positions (Rodenburg et al., 2007). At each scanning step, coherent diffraction patterns are recorded in the far field, and phase retrieval algorithms are used to reconstruct the complex-valued transmissivity of the specimen (Faulkner and Rodenburg, 2004). The combination of phase images acquired at different incident angles of the beam serve for 3D tomographic reconstruction of the specimen. As in CDI, the resolution in PXCT is only limited, in theory, by the largest diffraction angle at which intensities can be reliably detected, but in practice it is often limited by positioning accuracy. Moreover, with PXCT one can arbitrarily extend the field of view of the specimen, which is limited in plane-wave CDI, where the sample needs to be confined to a few micrometers in size due to the combination of a support constraint and a sampling requirement (Miao et al., 1998). Apart from a few reported experiments (Lima et al., 2009; Rodriguez et al., 2015), this limitation has hampered the application of CDI for cryo imaging, where surrounding ice layers are incompatible with a small, confined sample. Ptychographic algorithms with simultaneous reconstruction of the illumination (Guizar-Sicairos and Fienup, 2008; Thibault et al., 2008; Maiden and Rodenburg, 2009) are very robust to reconstruct thick objects producing phase shifts of many waves (da Silva et al., 2015) while keeping a high phase sensitivity of 0.005 rad (Lima et al., 2013). Therefore, the combination of X-ray ptychography with tomographic reconstruction results in high-quality 3D density maps (Diaz et al., 2012) which are increasingly used as a characterization tool in multiple scientific fields (da Silva et al., 2015; Chen et al., 2013; Fløystad et al., 2015; Dam et al., 2014). Using a recently developed instrument with high accuracy positioning, a resolution of 16 nm in 3D has been demonstrated (Holler et al., 2014). Ptychography has been successfully tested for 2D imaging of biological matter, both with freeze-dried (Giewekemeyer et al., 2010; Jones et al., 2014) and frozen-hydrated specimens (Lima et al., 2013; Deng et al., 2015), and for 3D imaging of freeze-dried specimens (Guizar-Sicairos et al., 2011; Wilke et al., 2012; Jones et al., 2013).

Here we demonstrate PXCT at an energy of 6.2 keV for 3D density mapping of frozen-hydrated biological matter. We show 3D maps of intact *Chlamydomonas* cells at 180 nm resolution with quantitative mass density values within 6% accuracy and with sufficient contrast to distinguish several organelles. Comparing with additional measurements on stained resin-embedded *Chlamydomonas* and earlier literature on EM and absorption X-ray microscopy, we identify the cell organelles and determine their mass densities in their hydrated state.

2. Materials and methods

2.1. Sample preparation

Chlamydomonas reinhardtii 137c wild type were obtained from the Chlamydomonas Genetic Center. Cells were cultured in Tris–acetate–phosphate (TAP) medium (Gorman and Levine, 1965). For the frozen-hydrated specimen preparation a quartz glass capillary of 1.20 mm outer diameter and 0.90 mm inner diameter was pulled to obtain a thin tip of about 7 μm diameter and tapering walls. After pulling, the capillary was fixed with glue to a standard 3 mm diameter brass pin from Hampton Research (CA, USA). Cells in their medium with a volume concentration of 8.5% glycerol as cryo-protectant were injected from the wide end of the capillary using a microliter syringe and needle, in such a way that the solution filled the thin part of the capillary up to the top. In Fig 1(b) we show a light microscope image of the confined cell solution in the microcapillary captured immediately before plunge freezing. The brass pin was then mounted in a sample mount with magnetic base from Hampton Research, and plunge frozen in liquid ethane. After plunging, the sample was stored in liquid nitrogen for a few days until the experiment took place.

For the preparation of the resin-embedded specimen, cells in liquid TAP medium were pelleted at 800 g for 8 min. The pellet

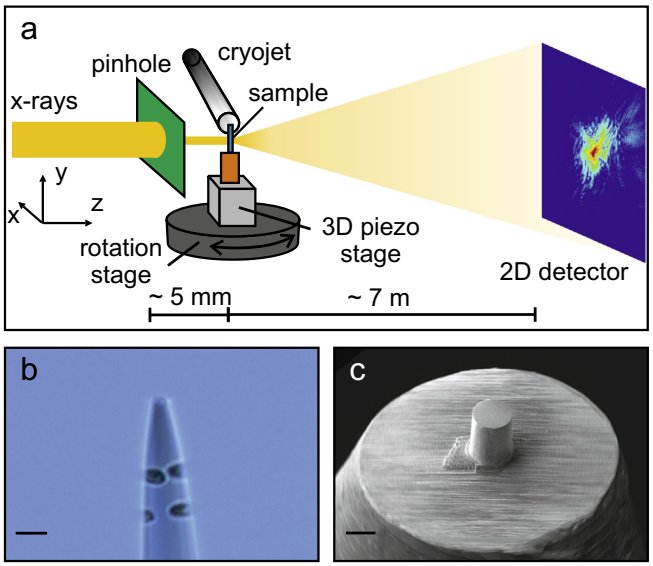

Fig.1. (a) Sketch of the setup used for ptychographic tomography measurements. (b) Light microscope image of *Chlamydomonas* specimen in solution confined in a glass microcapillary right before plunge freezing. (c) SEM image of stained, resin-embedded *Chlamydomonas* specimen prepared by focused ion beam (FIB). Scale bars in (b) and (c) are 20 μm.

was fixed at room temperature in M1 culture medium containing 2.5% glutaraldehyde, pH 7.2. After one hour the fixative solution was exchanged for a new solution of M1 culture medium with 0.2% tannic acid and 1% glutaraldehyde. After a rinse with distilled water the specimen was postfixed with 1% OsO_4 in distilled water at 4 °C for 40 min. After washes with distilled water the sample was prestained with 3% uranyl acetate in distilled water. About 50 µl of the cell pellet were then embedded in 100 µl agar and cropped to a volume of $3 \times 3 \times 3$ mm^3. The agar piece was washed in distilled water and dehydrated using a graduated series of ethanol with a final step in propylene oxide (PO). The samples where then infiltrated with araldite LX 112 with increasing volume concentrations of 33% araldite in PO (2 h), 67% in PO (2 h), and 100% araldite (overnight). Polymerization took place in fresh, pure araldite LX 112 for 72 h at 60 °C.

The resin block with the embedded cells was mounted onto a scanning electron microscopy (SEM) stub with conductive carbon cement and sputter-coated with 5 nm Au. The block surface was then imaged in a focused ion beam (FIB)-SEM FEI Helios 600i at the Scientific Center for Optical and Electron Microscopy at the ETH Zürich (ScopeM) with 20 kV electrons to localize areas with high cell density. A carbon deposition was placed over the selected region of interest. At this spot a cylinder of about 25 µm diameter was shaped by Ga ion milling. The cylinder was undercut by the ion beam and transferred with a micromanipulator onto a flat-top microtip for ptychographic tomography measurements, where it was attached and firmly mounted by platinum deposition. The pillar top with the initial carbon deposition was finally cut flat using the ion beam. In Fig. 1(c) we show an SEM image of the resin pillar mounted on the top of the holder.

2.2. Ptychographic tomography measurements and reconstructions

Ptychographic tomography measurements were done at the cSAXS beamline of the Swiss Light Source at the Paul Scherrer Institut in Villigen, Switzerland, using a photon energy of 6.2 keV. In Fig. 1(a) we show a sketch of the experimental setup. A pinhole of about 3 µm diameter was used to define the confined coherent illumination. The sample was placed about 5–6 mm downstream the pinhole, mounted on a 3D piezo-driven nanopositioning stage and a rotation stage for scanning in the xy plane at different incidence angles of the X-ray beam onto the sample. A cryo-jet was placed a few millimeters from the sample in such a way that gaseous N_2 at 110 K was continuously flowing over the sample. Coherent diffraction patterns were recorded with a Pilatus 2M detector (Kraft et al., 2009) with a pixel size of 172 µm placed about 7 m downstream the sample with a He-filled tube in between to reduce air scattering and absorption.

For the measurement of the frozen-hydrated specimen we placed the sample 5.3 mm dowstream the pinhole, which provided a flux of about 1.5×10^6 photons/s. Ptychographic scans were performed in a circular pattern (Dierolf et al., 2010) with a radial step size of 1.4 µm over a field of view of 40×30 µm^2 (horizontal × vertical) with a total number of 487 points. The acquisition time at each scanning position was 0.1 s and the total time employed for each scan was about 126 s. For each ptychographic scan we estimate that the incident number of photons per area was $N_0 = 8.7 \times 10^5$ photons/µm^2. Ptychographic scans were repeated at 360 rotation angles ranging from 0° to 179.5° with a constant angular step of 0.5° with the exception of one of the projections which was not measured due to a technical problem occurring during the measurement. The dose imparted on the sample was estimated as $D = \mu N_p N_0 \epsilon / \rho$ (Howells et al., 2009), where N_p is the number of angular projections, ϵ is the photon energy, and μ and ρ are the linear attenuation coefficient and the density of the specimen, respectively. The linear attenuation coefficient was obtained from tabulated values (Henke et al., 1993) assuming that the composition of the sample is mostly water. We obtained a value of $D = 6.7 \times 10^5$ Gy for the total dose imparted on the frozen-hydrated specimen.

The resin-embedded sample was placed at 5.7 mm away from the pinhole, which provided a flux of 8×10^5 photons/s in this experiment. At each rotation angle the sample was scanned at 565 positions in a grid of concentric circles with a radial step size of 1.3 µm and covering a field of view of 40×30 µm^2 (horizontal × vertical). At each position coherent diffraction patterns were recorded with an exposure time of 0.1 s, taking about 133 s to complete a full ptychographic scan and corresponding to $N_0 = 4.9 \times 10^5$ photons/µm^2. Scans at 288 angular positions with a step of 0.625° ranging from 0° to 179.375° were measured. We estimated a total dose of $D = 3.6 \times 10^5$ Gy on the specimen, assuming that it was composed of epoxy resin with the chemical composition given in Table 1 and 1.22 g/cm^3 density, as determined from the measurements reported below.

The diffraction patterns recorded for each ptychographic scan were used in an iterative phase retrieval algorithm in order to recover the 2D complex-valued transmission function of the specimen at each angular position. We selected 192×192 pixels of the detector centered around the direct beam, and ptychographic reconstructions were performed using 200 iterations of the difference map algorithm (Thibault et al., 2008; Thibault et al., 2009) followed by 100 iterations of a maximum likelihood refinement (Thibault and Guizar-Sicairos, 2012). For the frozen-hydrated specimen the distance between the sample and the detector was 7.212 m, resulting in ptychographic reconstructions with a pixel size of 43.64 nm, whereas in the experiment for the resin-embedded specimen the distance was 7.410 m and the pixel size of the reconstructed images was 44.87 nm. In both experiments the cryo-jet caused thermal drifts between the specimen and the pinhole within a ptychographic scan, which resulted in non-reproducible features on the hundred nanometer scale and limited the spatial resolution.

Phase projections were further processed to remove a phase offset and a linear phase term, which are intrinsic degrees of freedom in ptychographic reconstructions, and aligned in both x and y directions with subpixel precision using the method reported in reference Guizar-Sicairos et al. (2011). A refinement alignment in x based on tomographic consistency was further applied (Guizar-Sicairos et al., 2015). Finally, tomographic reconstructions were performed directly from wrapped phase projections by filtered back projection (FBP) as introduced in reference Guizar-Sicairos et al. (2011). During the filtering step of the FBP we used a Hanning filter with cutoff at 40% and 50% of the Nyquist sampling frequency for the frozen-hydrated and the resin-embedded specimen, respectively. These values were chosen such that noise was reduced without compromising the final 3D resolution, which was esti-

Table 1
Values of A/Z for some materials and representatives for material classes.

Substance	Chemical formula	A/Z (g/mol)
Water	H_2O	1.8015
Protein	$H_{50}C_{30}N_9O_{10}S_1$	1.8736
Lipid	$H_{98}C_{55}O_6$	1.7969
Starch	$C_6H_{10}O_5$	1.8854
Chromatin	$C_{38}H_{46}O_{24}N_{15}P_3$	1.9093
Epoxy resin	$C_{124}H_{185}O_{43}N_{0.4}$	1.8569
Quartz glass	SiO_2	2.0028

mated by 3D Fourier shell correlation (FSC). For the resolution estimation we produced two independent tomograms from half of the projections (Holler et al., 2014), computed the FSC, and compared it with the half-bit threshold criterion (van Heel and Schatz, 2005). In this way we estimated 3D resolutions of 180 nm and 150 nm for the frozen-hydrated and for the stained, resin-embedded specimen, respectively.

2.3. Quantitative mass density maps from phase tomography

Phase tomography provides the 3D distribution of the difference from unity of the real part of the refractive index of the sample, $\delta(\vec{r})$. It is sufficient to choose the incident X-ray energy away from any absorption edge of the elements in the sample to obtain a direct measurement of the 3D electron density distribution within the sample, $n_e(\vec{r})$. Furthermore, mass density values can be obtained from the electron density by

$$\rho(\vec{r}) = \frac{n_e(\vec{r})A}{N_A Z}, \quad (1)$$

where A is the molar mass, Z the total number of electrons in the molecule, and N_A denotes Avogadro's number. Although the mass density determination relies on the knowledge of the chemical composition of each part of the sample, in practice the ratio A/Z is close to 2 g/mol for most light atoms with the notable exception of hydrogen, for which $A/Z = 1$ g/mol. We show in Table 1 the estimated chemical content of some basic biological substances and their A/Z values, which range from 1.80 to 1.91 g/mol. Consequently phase tomography of hydrated biological tissue renders directly the 3D mass density distribution of the specimen with quantitative values within a range of 5.7%. The knowledge of the elemental composition of the specimen can reduce this uncertainty considerably, as discussed later.

2.4. Classification of organelles and segmentation

For each sample, organelles inside the cells were classified into different groups based on their morphology and densities:

1. High-density spherical or quasi-spherical organelles.
2. Grouped organelles of lower density.
3. Other smaller, isolated organelles with similar density as in group 2.
4. The rest of the cell region, with slightly higher density than the surrounding medium.
5. Large, spherical organelle with density values between those in group 1 and 4.
6. Large, spherical organelle with density equal to the surrounding medium.

Groups 5 and 6 were only found in the resin-embedded specimen. Segmentation of the organelles was done as detailed in Appendix A and, for each group in each sample, the average density value and the standard deviation were obtained for a quantitative density analysis.

3. Results

3.1. Three-dimensional density maps

Recording ptychographic projections over a full angular range of 180° enables the reconstruction of 3D electron density maps with accurate quantitative values (Diaz et al., 2012). In Fig. 2 we show two orthoslices through each of the tomograms, revealing the internal structure of each specimen. In the frozen-hydrated specimen (Figs. 2(a and b)) we distinguish the walls of the glass microcapillary with varying thickness from a few to several hundred nanometers and high electronic density of 0.66 electrons/Å^3 beyond the range of the chosen gray scale. Inside the capillary we observe two cells, probably the two upper cells in Fig. 1(b). The contrast between the cytoplasm in the cells and the surrounding ice matrix is very low but still detectable in this single slice of 43.64 nm thickness. Other high-density organelles within the cell are also observed. In Figs. 2(c and d) the stained resin-embedded specimen is shown. There is a clear contrast between the cytoplasm of the cells and the surrounding epoxy resin matrix, which results in a clear visualization of several cells within the 25 μm diameter pillar. Additionally, higher- and lower-density features from organelles inside the cells are also observed. On the top part of the pillar in Fig. 2(c) we observe the high-density layer deposited on the sample surface before the ion milling process.

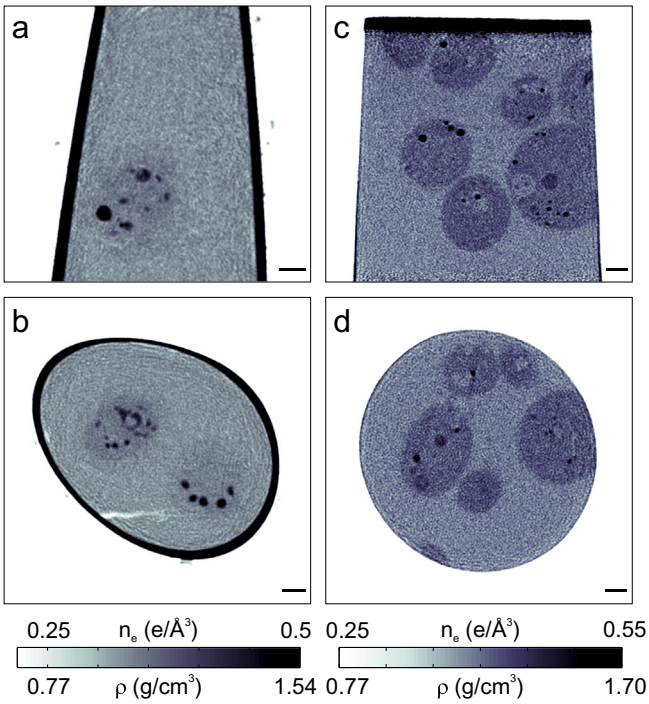

Fig.2. Orthoslices from tomographic reconstructions of *Chlamydomonas* cells. On the left we show slices from the frozen-hydrated cells confined in a glass microcapillary within the *xy* plane (a) and the *xz* plane (b); on the right side slices from the stained resin-embedded specimen are shown (c) and (d). Scale bars are 2 μm.

According to Eq. (1), with an estimate of A/Z we can convert electron to mass density. We have included the mass density values in the gray scales of Fig. 2 assuming $A/Z = 1.86$ g/mol, which is the same for epoxy resin and for the average value of the main materials found in plant biological specimens, namely water, protein, lipid, starch and chromatin (see Table 1). In the case of the resin-embedded specimen it is not easy to estimate the uncertainty introduced by this assumption because staining is a complex process which can be very different depending both on the biological substance and on the staining metal that has been used. On the other hand, in the frozen-hydrated specimen we estimate an uncertainty of about 6%, as discussed in Section 2.3.

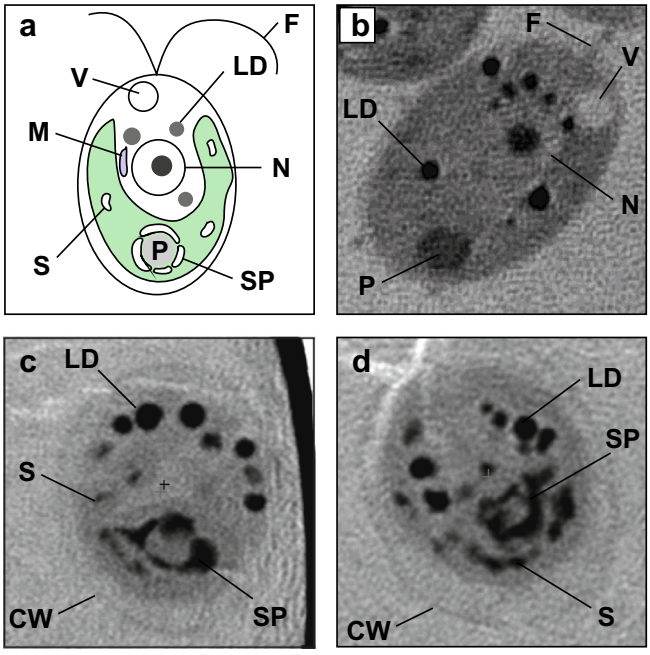

Fig.3. (a) Schematic structure of *Chlamydomonas* with the chloroplast in green. (b–d) Average of 20 slices with a total thickness of about 880 nm along planes cutting through the middle of the cells along their long axis for a stained, resin-embedded cell (b) and for two frozen-hydrated cells (c) and (d). Different organelles are labeled as vacuole (V), flagellum (F), lipid droplet (LD), nucleus with nucleolus (N), mitochondrion (M), pyrenoid (P), starch grain (S), starch platelets (SP) around pyrenoid, and cell wall (CW).

3.2. Segmentation and identification of organelles

The structure of a typical *Chlamydomonas* cell is sketched in Fig. 3(a). Most of the volume of the cell is occupied by the chloroplast, which is the organelle responsible for photosynthesis. On one extreme of the cell there is usually a contractile vacuole and two flagella, which are used for motion, and on the opposite side the pyrenoid is located, surrounded by starch platelets. Other starch grains can also be found in other parts of the chloroplast. In the middle there is the nucleus with nucleolus, typically surrounded by other organelles such as mitochondria or lipid droplets.

Inspection of average slices in planes along the long axis of the cells on the stained resin-embedded specimen in Fig. 3(b) allows the location of the different organelles in the cell: on one side of the cell we observe the contractile vacuole and the starting of the flagellum, on the opposite side we observe the region formed by the pyrenoid and surrounding starch grains, and in the middle the nucleus, from which probably only the nucleolus is visible, surrounded by high-density round organelles. Based on this we tentatively assign each classified group in Section 2.4 to a certain organelle type and will provide later arguments for this identification supported both by literature and density analysis: group 1 are probably lipid droplets (LD), group 2 starch platelets (SP) surrounding the pyrenoid, group 3 other isolated starch grains (S) scattered around the cell, group 4 the cytoplasm (C), group 5 the nucleolus (N) and group 6 vacuoles (V). Similar images of an average of 20 slices across the two cells in the frozen-hydrated specimen are shown in Fig. 3(c) and (d). Comparing with the stained, resin-embedded specimen it is not very

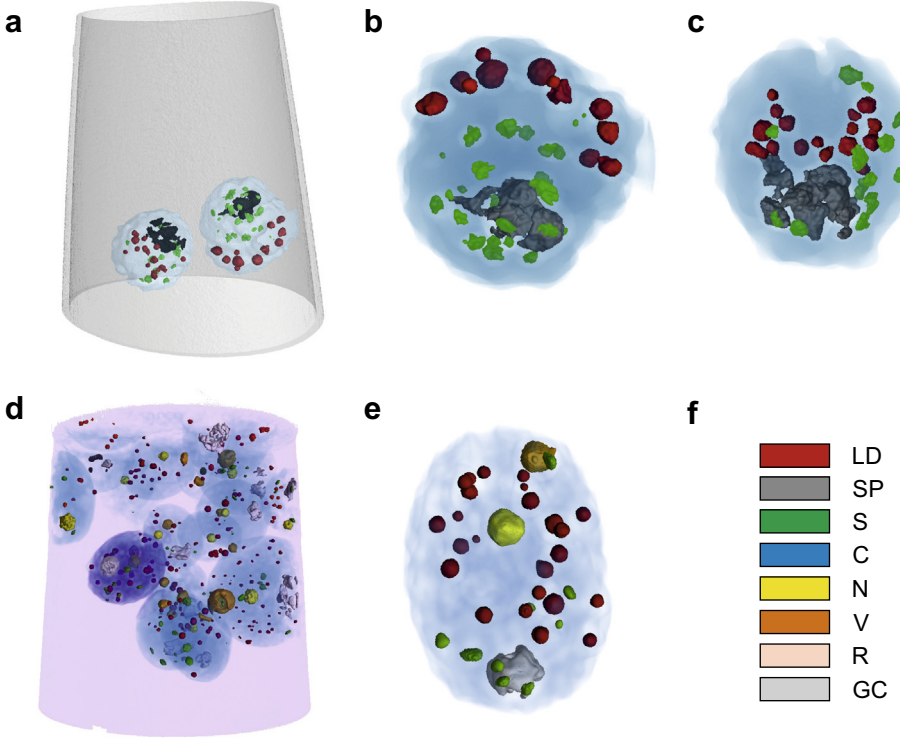

Fig.4. (a) 3D rendering of measured frozen-hydrated *Chlamydomonas* cells confined in a glass microcapillary. (b) and (c) Details of individual cells in (a) reoriented to compare with the cell in (e). (d) 3D rendering of measured stained resin-embedded specimen containing many *Chlamydomonas* cells. (e) Detail of one cell indicated in a darker blue tone in (d). (f) Color code of 3D rendering: lipid droplets (LD), starch platelets (SP) around pyrenoid, other starch grains (S), cytoplasm (C), nucleolus (N), vacuole (V), resin matrix (R), and glass capillary (GC).

Table 2
Average electron density, n_e (Å^{-3}), measured for each organelle group for frozen-hydrated and stained, resin-embedded *Chlamydomonas* specimens with upper and lower limits given by the standard deviation. Organelle groups are identified as lipid droplets (LD), starch platelets (SP) around the pyrenoid, other starch grains (S), cytoplasm (C), nucleolus (N), vacuole (V), matrix surrounding the cells, which is the solution medium in the frozen-hydrated specimen and epoxy resin (R) in the stained, resin-embedded specimen, and glass capillary (GC).

Group	Frozen-hydrated	Resin-embedded
LD	0.47 ± 0.03	0.56 ± 0.02
SP	0.430 ± 0.013	0.448 ± 0.002
S	0.415 ± 0.013	0.445 ± 0.003
C	0.345 ± 0.004	0.421 ± 0.002
N	NA	0.455 ± 0.03
V	NA	0.403 ± 0.001
Matrix	0.329 ± 0.003	0.397 ± 0.003
GC	0.66 ± 0.02	NA

Table 3
Mass density (average and standard deviation) measured for each organelle group of the frozen-hydrated *Chlamydomonas* specimen. For two-component regions a 0.5 M concentration is assumed. Values for matrix surrounding the cells are also provided.

Group	Composition	ρ (g/cm^3)
LD	Protein and lipid	1.42 ± 0.09
SP	Starch and water	1.34 ± 0.04
S	Starch and water	1.29 ± 0.04
C	Protein and water	1.072 ± 0.012
Ice matrix	Water	0.984 ± 0.009
GC	SiO_2	2.20 ± 0.07

straightforward to identify the organelles based on their location, but the previous assignment to organelle groups reveals lipid droplets, starch platelets surrounding the pyrenoid, and other starch grains.

We note that we find a nucleolus and a vacuole only in the resin-embedded specimen. The absence of nucleolus in the frozen-hydrated cells might be due to the condition of chromatin in the nucleus at the moment of freezing, such that the nucleolus offers no density contrast with respect to the surrounding matter.

Data segmentation enables 3D rendering of the data, as shown in Fig. 4, revealing the position and orientation of the cells in both samples and the position and orientation of the organelles within each cell. Details about the segmentation procedure can be found in Appendix A, including examples of data segmentation for each region and sample in Fig. 5. Apart from the organelle groups identified above, the resin matrix (R) in the resin-embedded specimen and the glass capillary (GC) containing the cell solution in the frozen-hydrated specimen are shown as well whereas rendering of the medium surrounding the frozen-hydrated cells is omitted for clarity. Segmentation further enables accurate quantification of the electron density of the different organelles. In Table 2 we show the results of averaging all voxels within each organelle group, where the specified upper and lower limits are given by the standard deviation. Here the matrix region corresponds to the epoxy resin for the resin-embedded specimen and the cell solution medium for the frozen-hydrated specimen.

In the following we support this identification of the organelles by analyzing their morphology and location within the cells and by comparison to the literature. Spherical dense organelles similar to those identified as lipid droplets were identified in TEM studies of stained *Chlamydomonas* (Moellering and Benning, 2010) and in frozen-hydrated unstained *Chlamydomonas* imaged by cryo soft X-ray microscopy (Hummel et al., 2012). The SP group resembles the starch grain arrangement typically found around the pyrenoid in TEM studies (Ohad et al., 1967). At the given resolution, the organelles in group S are too small for precise determination of their morphology. The similar density compared to the SP group supports the conjecture that they most likely are other starch grains scattered around the cell. Group C comprises the cytoplasm of the cells, having only a very weak contrast with respect to the surrounding medium of the cell both for the frozen-hydrated and the stained, resin-embedded specimens. The cytoplasm contains both chloroplast and cytosol, easily identified by TEM (Ohad et al., 1967) and soft X-ray microscopy (Hummel et al., 2012) because of element specific staining and X-ray absorption being a function of chemical composition, respectively. Even if the nuclear membrane is not clearly observed, the interpretation of N as nucleolus in the resin-embedded specimen is supported by a lower-density region surrounding the nucleolus, which can be observed in the orthoslice in Fig. 5(i). Finally, group V is identified as a vacuole because its density is very close to that in the surrounding resin matrix, assuming that the space inside the vacuole is mostly dominated by water. In the cells of the frozen-hydrated specimen no vacuoles were found.

3.3. Mass density determination of frozen-hydrated organelles

For accurate mass density determination of different organelles in the frozen-hydrated specimen we estimate an A/Z value for each particular organelle group according to their chemical composition. As material composition for the organelles we assume a 0.5 M concentration of two biological substances: protein and lipid in LD, starch and water in SP and S, and protein and water in C. For the ice matrix and the capillary we use the expected materials. The ratio A/Z is then computed from the values listed in Table 1 and used for the density determination according to Eq. (1). The results are summarized in Table 3.

4. Discussion

The results presented here demonstrate 3D hard X-ray microscopy of frozen-hydrated specimens with thickness larger than 10 μm. For comparison with other established techniques, we chose as specimen *Chlamydomonas* cells, which are thin enough for soft X-ray microscopy in the water window and for which higher-resolution 3D images have been reported (Hummel et al., 2012). A practical difficulty of ptychographic imaging is that scanning with an accuracy comparable with the aimed resolution is needed, which imposes higher stability requirements compared to full-field microscopy techniques aiming at the same resolution. This is especially challenging for 3D imaging since distortions in the images caused by positioning errors may be visually negligible in 2D but contribute to an overall decrease of resolution when combining all the projections in the tomographic reconstruction. Although in principle PXCT at 6.2 keV could achieve much higher resolution, in our experiment resolution was limited by mechanical instabilities and thermal drifts caused by the cryo-jet. In a recent experiment *Chlamydomonas* cells were imaged by X-ray ptychography in 2D at 26 nm resolution (Deng et al., 2015), which shows the potential of the technique once the appropriate instrumentation is developed.

PXCT provides a 3D density map of the specimen with accurate absolute values, as demonstrated in reference Diaz et al. (2012) by

obtaining an accurate measurement in a polystyrene sphere of known density. For the experiments discussed here, the density measured in the capillary confining the frozen-hydrated specimen, shown in Table 3, is in full agreement with that expected for quartz glass. The measured density of the ice matrix is 0.98 g/cm^3, assuming that its composition is mainly water. This is a reasonable result considering that the expected density for hyperquenched amorphous pure water is 0.94 g/cm^3 and that the liquid solution medium with 8.5% volume concentration of glycerol is expected to have a slightly higher density than water.

Although very faint and almost invisible in single slices, averaging of 20 slices in frozen-hydrated *Chlamydomonas* reveals a rim around the cells which we attribute to the cell wall, as seen in Fig. 3(c) and (d). The cell wall thickness is typically about 100 nm, as observed by TEM (Ohad et al., 1967). Given that the resolution in the 3D tomogram is 180 nm in 3D partial volume effects reduce the contrast, making its visualization difficult in a single slice. We believe that the reason for not observing a cell wall in the resin-embedded specimen is that it is spatially very close to the cytoplasm and, at the current resolution, it can't be distinguished due to partial-volume effects.

The identification of the organelle groups in the frozen-hydrated sample reduces considerably the uncertainty in the conversion from electron to mass density values. Even assuming a rather conservative spread in the molar concentration of the two components in the organelle material from 0.1 to 0.9, we estimate a maximum uncertainty of about 1% in the quantitative mass density values.

The highest density in frozen-hydrated *Chlamydomonas* is found in LD with a value of 1.42 g/cm^3. This is surprising because lipids typically have a mass density lower than water, and a density of 1.15 g/cm^3 would be expected for a 0.5 M concentration of protein and lipid mixture. A density of 1.10 g/cm^3 has been reported for lipid droplets measured by equilibrium density-gradient centrifugation (Takamori et al., 2006), but to the best of our knowledge higher values have not been reported. Water-window X-ray microscopy of *Chlamydomonas* (Weiβ et al., 2000; Hummel et al., 2012) reveal lipid droplets with strong contrast. However, since absorption contrast is sensitive to both density and chemical composition, from these results alone it is not possible to conclude that lipid droplets have a high mass density. In EM lipid droplets also feature rather strong contrast (Moellering and Benning, 2010) because osmium tetroxide binds preferentially to lipids (Plattner and Zingsheim, 1987). Similarly, this may explain the very high electron density we have determined in the LD group of the stained, resin-embedded specimen. Among these techniques only non-resonant X-ray phase tomography of frozen-hydrated specimens provides an unambiguous measurement of the mass density of lipid droplets in their native state.

For starch we measured a density of 1.34 g/cm^3 and 1.29 g/cm^3 for SP and S, respectively, which lies within the range of values reported in the literature (Yoon and Lim, 2003; Pérez and Bertoft, 2010). This range from 1.23 g/cm^3 to 1.5 g/cm^3 is quite large most probably due to the diversity of glucose branching, related to the percentage of amylose and amylopectin. In addition, this variability might be due to the fact that most studies have measured the density in vitro on purified starch. Note that organelle groups S and SP have the same electron density in frozen-hydrated and in stained, resin-embedded specimens, as shown in Table 2. Since starch is not easily stained by osmium tetroxide, nor by uranyl acetate, this supports the argument of S and SP being mostly comprised of starch.

Finally, in the C region we measured a density of 1.072 g/cm^3, only slightly higher than the ice matrix but still sufficient for reliable segmentation. Assuming that the non-hydrated content of the cytoplasm is protein of density 1.35 g/cm^3 (Howells et al., 2009), this means that we measure a dry weight concentration of 0.259, which can be directly compared with values found in earlier STEM work for the cytoplasm of liver cells of 0.26 (Zierold, 1988) and 0.247 (Sun et al., 1995).

In conclusion we have demonstrated absolute mass density mapping of frozen-hydrated *Chlamydomonas* cells with isotropic 3D resolution of 180 nm, in which the uncertainty of about 6% in the quantitative results stem primarily from the conversion from electron to mass density. Identifying different organelle groups inside the cells and using the knowledge of their chemical composition, the uncertainty in the mass density assessment was reduced to 1%. This proof of principle experiment has been conducted on individual cells in buffer solution confined in a microcapillary of 18 μm-diameter. The full understanding of biological systems requires structural information on all length scales. Mass density maps provided by X-ray phase nanotomography link the nowadays available molecular information to the nano and microscale, opening new possibilities to probe higher-order packing of molecules in context with the rest of the cell or tissue in which they are embedded, like for example the packing of chromatin in nuclei or the packing of thylakoid membranes in the chloroplast. The method employed here, ptychographic X-ray computed tomography (PXCT), allows the investigation of tissue specimens with thicknesses of many tens of micrometers, for which sample preparation protocols including high-pressure freezing and cryo-FIB are under development. With an instrument with a cryo-stage and laser interferometry-controllers (Holler et al., 2014; Holler and Raabe, 2015) with position accuracy down to 10 nm currently being commissioned, we expect that extended frozen-hydrated biological tissue will be imaged with much better resolution in the near future.

Acknowledgments

We thank Xavier Donath for technical support at the cSAXS beamline, Hans-Christian Stadler for the implementation of fast computer codes for ptychographic reconstructions, and Barbara Pfister and Samuel Zeeman for helpful discussions.

Appendix A. Data segmentation

Data segmentation was done using the commercial software VGStudio MAX. For each organelle we selected a seed region and applied a region growing algorithm to detect the border. For segmentation of all organelle groups except the lipid droplets (LD) in the stained, resin-embedded specimen and of the cytoplasm (C) in the frozen-hydrated specimen, data were treated beforehand using a smoothing, edge preserving filter. In Fig. 5 we show examples of region segmentation for all cases, comparing an orthoslice extracted from the 3D dataset on the right with the same slice indicating the segmented regions in colors on the left.

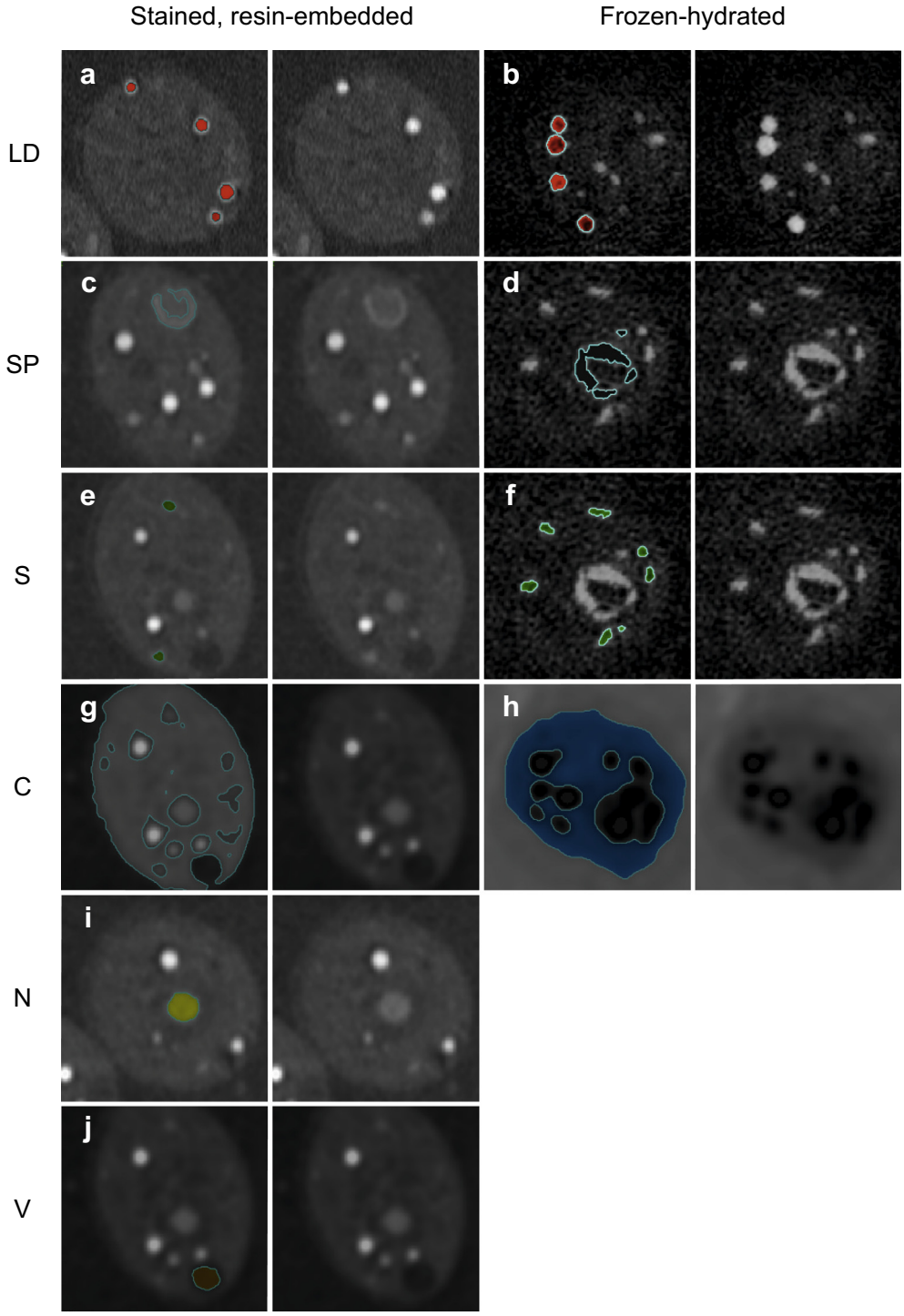

Fig.5. Orthoslices through the tomograms to show segmentation of different regions. The two columns on the left correspond to the stained, resin-embedded specimen, the two columns on the right correspond to the frozen-hydrated specimen, and each row corresponds to a different region. For each case we show on the right side an orthoslice through the 3D data and on the left side the same slice with the segmented region marked in color. Note that, depending on each case, the 3D data have been filtered as explained in the main text.

References

Adrian, M., Dubochet, J., Lepault, J., McDowall, A.W., 1984. Cryo-electron microscopy of viruses. Nature 308, 32–36.

Al-Amoudi, A., Studer, D., Dubochet, J., 2005. Cutting artefacts and cutting process in vitreous sections for cryo-electron microscopy. J. Struct. Biol. 150, 109–121.

Chen, B., Guizar-Sicairos, M., Xiong, G., Shemilt, L., Diaz, A., Nutter, J., Burdet, N., Huo, S., Mancuso, J., Monteith, A., Vergeer, F., Burgess, A., Robinson, I., 2013. Three-dimensional structure analysis and percolation properties of a barrier marine coating. Sci. Rep. 3, 1177.

Chichón, F.J., Rodríguez, M.J., Pereiro, E., Chiappi, M., Perdiguero, B., Guttmann, P., Werner, S., Rehbein, S., Schneider, G., Esteban, M., Carrascosa, J.L., 2012. Cryo X-ray nano-tomography of vaccinia virus infected cells. J. Struct. Biol. 177, 202–211.

Cloetens, P., Ludwig, W., Baruchel, J., Van Dyck, D., Van Landuyt, J., Guigay, J.P., Schlenker, M., 1999. Holotomography: quantitative phase tomography with micrometer resolution using hard synchrotron radiation x rays. Appl. Phys. Lett. 75, 2912–2914.

Dam, H.F., Andersen, T.R., Pedersen, E.B.L., Thydén, K.T.S., Helgesen, M., Carlé, J.E., Jørgensen, P.S., Reinhardt, J., Søndergaard, R.R., Jørgensen, M., Bundgaard, E.,

Krebs, Andreasen, J.W., . Enabling flexible polymer tandem solar cells by 3D ptychographic imaging. Adv. Energy Mater. 5, 1400736.
da Silva, J.C., Trtik, P., Diaz, A., Holler, M., Guizar-Sicairos, M., Raabe, J., Bunk, O., Menzel, A., 2015. Mass density and water content of saturated never-dried calcium silicate hydrates. Langmuir 31, 3779–3783.
Deng, J., Vine, D.J., Chen, S., Nashed, Y.S.G., Jin, Q., Phillips, N.W., Peterka, T., Ross, R., Vogt, S., Jacobsen, C.J., 2015. Simultaneous cryo X-ray ptychographic and fluorescence microscopy of green algae. Proc. Natl. Acad. Sci. USA 112, 2314–2319.
Diaz, A., Trtik, P., Guizar-Sicairos, M., Menzel, A., Thibault, P., Bunk, O., 2012. Quantitative X-ray phase nanotomography. Phys. Rev. B 85, 020104(R).
Dierolf, M., Menzel, A., Thibault, P., Schneider, P., Kewish, C.M., Wepf, R., Bunk, O., Pfeiffer, F., 2010. Ptychographic X-ray computed tomography at the nanoscale. Nature 467, 436–440.
Faulkner, H.M.L., Rodenburg, J.M., 2004. Movable aperture lensless transmission microscopy: a novel phase retrieval algorithm. Phys. Rev. Lett. 93, 023903.
Fløystad, J.B., Skjønsfjell, E.T.B., Guizar-Sicairos, M., Høydalsvik, K., He, J., Andreasen, J.W., Zhang, Z., Breiby, D.W., 2015. Quantitative 3D X-ray imaging of densification, delamination and fracture in a micro-composite under compression. Adv. Eng. Mater. 17, 545–553.
Giewekemeyer, K., Thibault, P., Kalbfleisch, S., Beerlink, A., Kewish, C.M., Dierolf, M., Pfeiffer, F., Salditt, T., 2010. Quantitative biological imaging by ptychographic X-ray diffraction microscopy. Proc. Natl. Acad. Sci. USA 107, 529–534.
Gorman, D.S., Levine, R.P., 1965. Cytochrome f and plastocyanin: their sequence in the photosynthetic electron transport chain of Chlamydomonas reinhardi. Proc. Natl. Acad. Sci. USA 54, 1665–1669.
Guizar-Sicairos, M., Fienup, J.R., 2008. Phase retrieval with transverse translation diversity: a nonlinear optimization approach. Opt. Express 16, 7264–7278.
Guizar-Sicairos, M., Diaz, A., Holler, M., Lucas, M.S., Menzel, A., Wepf, R.A., Bunk, O., 2011. Phase tomography from X-ray coherent diffractive imaging projections. Opt. Express 19, 21345–21357.
Guizar-Sicairos, M., Boon, J.J., Mader, K., Diaz, A., Menzel, A., Bunk, O., 2015. Quantitative interior X-ray nanotomography by a hybrid imaging technique. Optica 2, 259–266.
Hanssen, E., Knoechel, C., Dearnley, M., Dixon, M.W.A., Le Gros, M., Larabell, C., Tilley, L., 2012. Soft X-ray microscopy analysis of cell volume and hemoglobin content in erythrocytes infected with asexual and sexual stages of *Plasmodium falciparum*. J. Struct. Biol. 177, 224–232.
Helmstaedter, M., Briggman, K.L., Denk, W., 2008. 3D structural imaging of the brain with photons and electrons. Curr. Opin. Neurobiol. 18, 633–641.
Henke, B.L., Gullikson, E.M., Davis, J.C., 1993. X-ray interactions: photoabsorption, scattering, transmission, and reflection at $E = 50–30000$ eV, $Z = 1–92$. Atom. Data Nucl. Data 54, 181–342.
Holler, M., Raabe, J., 2015. Error motion compensating tracking interferometer for the position measurement of objects with rotational degree of freedom. Opt. Eng. 54, 054101.
Holler, M., Diaz, A., Guizar-Sicairos, M., Karvinen, P., Färm, E., Härkönen, E., Ritala, M., Menzel, A., Raabe, J., Bunk, O., 2014. X-ray ptychographic computed tomography at 16 nm isotropic 3D resolution. Sci. Rep. 4, 3857.
Howells, M.R., Beetz, T., Chapman, H.N., Cui, C., Holton, J.M., Jacobsen, C.J., Kirz, J., Lima, E., Marchesini, S., Miao, H., Sayre, D., Shapiro, D.A., Spence, J.C.H., Starodub, D., 2009. An assessment of the resolution limitation due to radiation-damage in X-ray diffraction microscopy. J. Electron Spectrosc. 170, 4–12.
Hummel, E., Guttmann, P., Werner, S., Tarek, B., Schneider, G., Kunz, M., Frangakis, A. S., Westermann, B., 2012. 3D ultrastructural organization of whole *Chlamydomonas reinhardtii* cells studied by nanoscale soft X-ray tomography. PLOS One 7, e53293.
Jiang, H., Song, C., Chen, C.-C., Xu, R., Raines, K.S., Fahimian, B.P., Lu, C.-H., Lee, T.-K., Nakashima, A., Urano, J., Ishikawa, T., Tamanoi, F., Miao, J., 2010. Quantitatie 3D imaging of whole, unstained cells by using X-ray diffraction microscopy. Proc. Natl. Acad. Sci. USA 107, 11234–11239.
Jones, M.W.M., van Riessen, G.A., Abbey, B., Putkunz, C.T., Junker, M.D., Balaur, E., Vine, D.J., McNulty, I., Chen, B., Arhatari, B.D., Frankland, S., Nugent, K.A., Tilley, L., Peele, A.G., 2013. Whole-cell phase contrast imaging at the nanoscale using Fresnel coherent diffractie imaging tomography. Sci. Rep. 3, 2288.
Jones, M.W.M., Elgass, K., Junker, M.D., Luu, M.B., Ryan, M.T., Peele, A.G., van Riessen, G.A., 2014. Mapping biological composition through quantitative phase and absorption X-ray ptychography. Sci. Rep. 4, 6796.
Kraft, P., Bergamaschi, A., Brönnimann, C., Dinapoli, R., Eikenberry, E.F., Graafsma, H., Henrich, B., Johnson, I., Kobas, M., Mozzanica, A., Schlepütz, C.M., Schmitt, B., 2009. Characterization and calibration of PILATUS detectors. IEEE Trans. Nucl. Sci. 56, 758–764.
Leis, A., Rockel, B., Andrees, L., Baumeister, W., 2009. Visualizing cells at the nanoscale. Trends Biochem. Sci. 34, 60–70.
Lima, E., Wiegart, L., Pernot, P., Howells, M., Timmins, J., Zontone, F., Madsen, A., 2009. Cryogenic X-ray diffraction microscopy for biological samples. Phys. Rev. Lett. 103, 198102.
Lima, E., Diaz, A., Guizar-Sicairos, M., Gorelick, S., Pernot, P., Schleier, T., Menzel, A., 2013. Cryo-scanning X-ray diffraction microscopy of frozen-hydrated yeast. J. Microsc. 249, 1–7.
Maiden, A.M., Rodenburg, J.M., 2009. An improved ptychographical phase retrieval algorithm for diffractive imaging. Ultramicroscopy 109, 1256–1262.
Miao, J., Sayre, D., Chapman, H.N., 1998. Phase retrieval from the magnitude of the Fourier transforms of nonperiodic objects. J. Opt. Soc. Am. A 15, 1662–1669.
Moellering, E.R., Benning, C., 2010. RNA interference silencing of a major lipid droplet protein affects lipid droplet size in *Chlamydomonas reinhardtii*. Eukaryot. Cell 9, 97–106.
Ohad, I., Siekevitz, P., Palade, G.E., 1967. Biogenesis of chloroplast membranes. I. Plastid dedifferentiation in a dark-grown algal mutant (*Chlamydomonas reinhardi*). J. Cell Biol. 35, 521–552.
Parkinson, D.Y., McDermott, G., Etkin, L.D., Le Gros, M.A., Larabell, C.A., 2008. Quantitative 3D imaging of eukaryotic cells using soft X-ray tomography. J. Struct. Biol. 162, 380–386.
Pérez, S., Bertoft, E., 2010. The molecular structures of starch components and their contribution to the architecture of starch granules: a comprehensive review. Starch 62, 389–420.
Plattner, H., Zingsheim, H.-P., 1987. Elektronenmikroscopische Methodik in der Zell- und Molekularbiologie. Fischer.
Rodenburg, J.M., Hurst, A.C., Cullis, A.G., Dobson, B.R., Pfeiffer, F., Bunk, O., David, C., Jefimovs, K., Johnson, I., 2007. Hard-X-ray lensless imaging of extended objects. Phys. Rev. Lett. 98, 034801.
Rodriguez, J.A., Xu, R., Chen, C.-C., Huang, Z., Jiang, H., Chen, A.L., Raines, K.S., Prior, A., Nam, D., Wiegart, L., Song, C., Madsen, A., Chuskin, Y., Zontone, F., Bradley, P. J., Miao, J., 2015. Three-dimensional coherent X-ray diffractive imaging of whole frozen-hydrated cells. IUCrJ 2, 575–583.
Schneider, G., Guttmann, P., Heim, S., Rehbein, S., Mueller, F., Nagashima, K., Heymann, J.B., Müller, W.G., McNally, J.G., 2010. Three-dimensional cellular ultrastructure resolved by X-ray microscopy. Nat. Methods 7, 985–987.
Stampanoni, M., Mokso, R., Marone, F., Vila-Comamala, J., Gorelick, S., Trtik, P., Jefimovs, K., David, C., 2010. Phase-contrast tomography at the nanoscale using hard X-rays. Phys. Rev. B 81, 140105(R).
Sun, S.Q., Shi, S.-L., Hunt, J.A., Leapman, R.D., 1995. Quantitative water mapping of cryosectioned cells by electron energy-loss spectroscopy. J. Microsc.-Oxford 177, 18–30.
Takamori, S., Holt, M., Stenius, K., Lemke, E.A., Grnborg, M., Riedel, D., Urlaub, H., Schenck, S., Brügger, B., Ringler, P., Müller, S.A., Rammner, B., Gräter, F., Hub, J.S., De Groot, B.L., Mieskes, G., Moriyama, Y., Klingauf, J., Grubmüller, H., Heuser, J., Wieland, F., Jahn, R., 2006. Molecular anatomy of a trafficking organelle. Cell 127, 831–846.
Thibault, P., Guizar-Sicairos, M., 2012. Maximum-likelihood refinement for coherent diffractive imaging. New J. Phys. 14, 063004.
Thibault, P., Dierolf, M., Menzel, A., Bunk, O., David, C., Pfeiffer, F., 2008. High-resolution scanning X-ray diffraction microscopy. Science 321, 379–382.
Thibault, P., Dierolf, M., Bunk, O., Menzel, A., Pfeiffer, F., 2009. Probe retrieval in ptychographic coherent diffractive imaging. Ultramicroscopy 109, 338–343.
van Heel, M., Schatz, M., 2005. Fourier shell correlation threshold criteria. J. Struct. Biol. 151, 250–262.
von Zglinicki, T., Bimmler, M., 1987. The intracellular distribution of ions and water in rat liver and heart muscle. J. Microsc. 146, 77–85.
Weiβ, D., Schneider, G., Niemann, B., Guttmann, P., Rudolph, D., Schmahl, G., 2000. Computed tomography of cryogenic biological specimens based on X-ray microscopic images. Ultramicroscopy 84, 185–197.
Wilke, R.N., Priebe, M., Bartels, M., Giewekemeyer, K., Diaz, A., Karvinen, P., Salditt, T., 2012. Hard X-ray imaging of bacterial cells: nano-diffraction and ptychographic reconstruction. Opt. Express 20, 19232–19254.
Yoon, J.-W., Lim, S.-T., 2003. Molecular fractionation of starch by density-gradient ultracentrifugation. Carbohydr. Res. 338, 611–617.
Zierold, K., 1988. X-ray microanalysis of freeze-dried and frozen-hydrated cryosections. J. Electron Microsc. Tech. 9, 65–82.